Tidal flow over three-dimensional topography in a stratified fluid

Benjamin King, H. P. Zhang, and Harry L. Swinney
Center for Nonlinear Dynamics and Department of Physics, The University of Texas at Austin, Austin, Texas 78712, USA

(Received 18 May 2009; accepted 21 September 2009; published online 9 November 2009)

Our laboratory experiments and numerical simulations of stratified tidal flow past model topography (a half sphere on a horizontal plane) reveal several three-dimensional flow features, including an unexpected flow perpendicular to the forcing plane (the vertical plane through the center of the sphere, in the direction of the oscillating tide). This perpendicular flow has a time-independent component and a component oscillating at twice the tidal frequency. Our results show that the time-independent part of the perpendicular flow forms a large-scale horizontal circulation, which could enhance material transport and mixing near bottom topography in the oceans. In addition, for small forcing amplitude we find that the azimuthal dependence of the internal wave field is described by the functional form cos ϕ, as predicted by linear inviscid theory. At higher forcing amplitude, the internal wave energy is more concentrated in the forcing direction. Finally, we observe a wave intensity asymmetry in the polar direction and explain the asymmetry using a geometrical argument. © *2009 American Institute of Physics*. [doi:10.1063/1.3253692]

I. INTRODUCTION

To maintain the observed global ocean circulation, roughly 2 TW of power is required to mix the deep ocean[1] and to bring cool dense water from great depths to the surface. While the magnitude of the required mixing energy is known, the source of this energy is poorly understood. A significant amount of mixing is probably caused by breaking internal gravity waves which, through a cascade of length scales, transfer large-scale tidal motion into internal waves and eventually into small-scale overturning and mixing when the internal waves break.[2–4] About half of the internal wave energy is generated by oscillating tidal flow past bottom topography such as ridges and seamounts; the other half is generated by wind forcing at the surface.[5]

Much work has been done to characterize the generation of internal waves by two-dimensional (2D) topography in the laboratory,[6–10] numerical simulations,[11–23] and field observations.[2,24–27] In the nonrotating 2D case, oscillating flow past idealized topography such as a cylinder results in four wavebeams that satisfy the following dispersion relation:

$$\frac{\omega}{N} = \sin \alpha, \tag{1}$$

where α is the angle of the group velocity vector, measured from the horizontal, ω is the tidal frequency, and N is the buoyancy frequency, defined as $N=\sqrt{-(g/\rho_o)(d\rho/dz)}$ with $d\rho/dz$ being the density gradient and ρ_o a constant reference density. The four wavebeams comprise the familiar St. Andrew's cross pattern first observed by Mowbray and Rarity.[28]

While the 2D case offers some insight into internal wave generation in the ocean, most bottom topography is three dimensional (3D), and even quasi-2D features such as ridges have end effects and 3D roughness. For this reason, it is important to examine waves generated in a 3D system. Two recent experiments have examined the 3D internal wave fields generated by vertically oscillating spheres. Flynn and Sutherland[29] studied this case and developed a viscous theory based on the procedure of Hurley and Keady,[6] and Weidman and Peacock[30] studied the problem with rotation included. In contrast to the 2D cases where the wave characteristics form a cross, in 3D the characteristics are conical surfaces along which the dispersion relation (1) allows waves to propagate (Fig. 1).

The case of a horizontally oscillating sphere, which we consider here, is more relevant to the oceans than the case of vertically oscillating spheres. Horizontal tidal flows over complex 3D topography generate complicated internal wave patterns that are studied by oceanographers in experiments and simulations. Holloway and Merrifield[31] examined a horizontally oscillating flow and found that for topography with a long aspect ratio (defined for a 3D Gaussian mountain as the ratio of the longest horizontal dimension to the shortest horizontal dimension), flow incident perpendicular to the long direction of the topography generates internal waves more efficiently than when the topography has low aspect ratio. This is reasonable since the flow must go over long (quasi-2D) topography, resulting in larger vertical velocities and stronger internal waves. In another study, Munroe and Lamb[32] looked at internal wave energy flux as a function of topographic height and slope. They found that the directional dependence of the energy flux depends on both the height and horizontal aspect ratio of the topography. Another relevant study is the linear theory analysis of Baines,[33] who modeled tidal flow over a pillbox, and obtained an internal wave field similar to that reported in this work. Baines commented briefly on the azimuthal dependence of the internal wave field, which we discuss in detail later.

The only analysis of the horizontally oscillating sphere

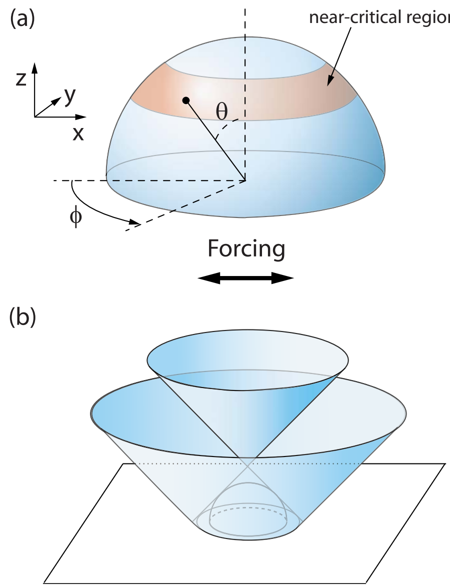

FIG. 1. (Color online) (a) Horizontally oscillating tidal flow (in the x direction) impinges on a half sphere. The azimuthal angle ϕ is measured from the x-axis and the polar angle θ from the vertical. The dark band denotes the near-critical region where the internal wave generation is most intense (see text). (b) Internal waves are allowed by the dispersion relation [Eq. (1)] to propagate along two nested cones, the upper one corresponding to waves propagating upward from the near-critical region and the lower cone corresponding to waves that propagate downward from the near-critical region and are reflected from the horizontal plane ($z=0$).

was that of Appleby and Crighton,[34] who solved the linear, inviscid problem for $\omega > N$ and then used analytic continuation to obtain near- and far-field solutions for the $\omega < N$ case, in which internal waves can propagate.

We examine the generation of internal waves by 3D topography for a system that shares qualitative features with supercritical topography on the ocean floor: a horizontally oscillating flow over a half sphere (Fig. 1). The half sphere is taken to be centered at the origin; z is in the vertical direction (antiparallel to the gravity vector), x is in the forcing direction, and y is the remaining coordinate in the right-handed triad. The azimuthal angle ϕ is measured from the x-axis. The polar angle θ [as in Eq. (1)] is measured from the vertical. Internal waves are generated most intensely when the slope of wavebeam propagation is near the slope of the topography. As in recent work, we define a *near-critical* region to be where the topographic slope differs from $\cot\theta$ by no more than 0.09.[18]

Our experiments and numerical simulations yield internal waves that are more intense in the forcing direction ($\phi=0$) than in other directions, which is not surprising. However, it was surprising to find, perpendicular to the forcing direction, a strong nonlinear flow that arises from higher harmonic oscillations in the boundary layer around the half sphere. This flow is absent in unstratified flows, as well as in stratified flows where $\omega > N$ and internal waves do not propagate.

This paper is organized as follows: Sec. II discusses the numerical simulations and laboratory experiments, Sec. III presents the internal wave structure and asymmetry between the wavebeams, Sec. IV describes the out-of-forcing plane nonlinear flow, and Sec. V summarizes the results and discusses their relevance to ocean flows.

II. METHODS

A. Numerical simulations

All numerical simulations are performed using CDP 2.4, a large eddy simulation code developed by Ham[35] at the Center for Integrated Turbulence Simulations at Stanford University. We turn off all subgrid-scale modeling, making it a direct numerical simulation. CDP is a parallel, unstructured finite-volume-based solver modeled on the algorithm presented in Ref. 36 with some modifications.[35] The code utilizes a fractional step time marching scheme and several implicit schemes for the spatial operators[37] to obtain second-order accuracy in space and time. CDP solves the following system of equations for the velocity field components (u,v,w) in the (x,y,z) directions (see Fig. 1):

$$\frac{\partial u}{\partial t} + u\frac{\partial u}{\partial x} + v\frac{\partial u}{\partial y} + w\frac{\partial u}{\partial z} = -\frac{1}{\rho_o}\frac{\partial p}{\partial x} + \frac{\mu}{\rho_o}\left(\frac{\partial^2}{\partial x^2} + \frac{\partial^2}{\partial y^2} + \frac{\partial^2}{\partial z^2}\right)u, \tag{2}$$

$$\frac{\partial v}{\partial t} + u\frac{\partial v}{\partial x} + v\frac{\partial v}{\partial y} + w\frac{\partial v}{\partial z} = -\frac{1}{\rho_o}\frac{\partial p}{\partial y} + \frac{\mu}{\rho_o}\left(\frac{\partial^2}{\partial x^2} + \frac{\partial^2}{\partial y^2} + \frac{\partial^2}{\partial z^2}\right)v, \tag{3}$$

$$\frac{\partial w}{\partial t} + u\frac{\partial w}{\partial x} + v\frac{\partial w}{\partial y} + w\frac{\partial w}{\partial z} = -\frac{1}{\rho_o}\frac{\partial p}{\partial z} + \frac{\mu}{\rho_o}\left(\frac{\partial^2}{\partial x^2} + \frac{\partial^2}{\partial y^2} + \frac{\partial^2}{\partial z^2}\right)w + \frac{\rho}{\rho_o}g, \tag{4}$$

$$\frac{\partial u}{\partial x} + \frac{\partial v}{\partial y} + \frac{\partial w}{\partial z} = 0, \tag{5}$$

$$\frac{\partial \rho}{\partial t} + u\frac{\partial \rho}{\partial x} + v\frac{\partial \rho}{\partial y} + w\frac{\partial \rho}{\partial z} = D\left(\frac{\partial^2}{\partial x^2} + \frac{\partial^2}{\partial y^2} + \frac{\partial^2}{\partial z^2}\right)\rho. \tag{6}$$

Equations (2)–(4) are the Navier–Stokes equations written in the Boussinesq approximation, Eq. (5) is the continuity equation, and Eq. (6) is the density advection-diffusion equation. The density of the fluid is ρ and ρ_o is a reference density, taken to be 1 $\mathrm{g/cm^3}$. For the dynamic viscosity μ, we use the value for water, $\mu=0.01$ $\mathrm{g\ cm^{-1}\ s^{-1}}$. The density diffusion coefficient D, taken to be 10^{-9} $\mathrm{cm^2\ s^{-1}}$ for all simulations discussed in this study, is so small as to make the diffusion time scale many orders of magnitude longer than a typical simulation. This is an accurate representation of our experiments, where the molecular diffusion time scale of the salt (and hence the density diffusion time scale) is on the order of months.

To utilize CDP, a grid must be generated for the computational domain. POINTWISE GRIDGEN (Pointwise, Inc., www.pointwise.com) is used to generate all of the grids. The

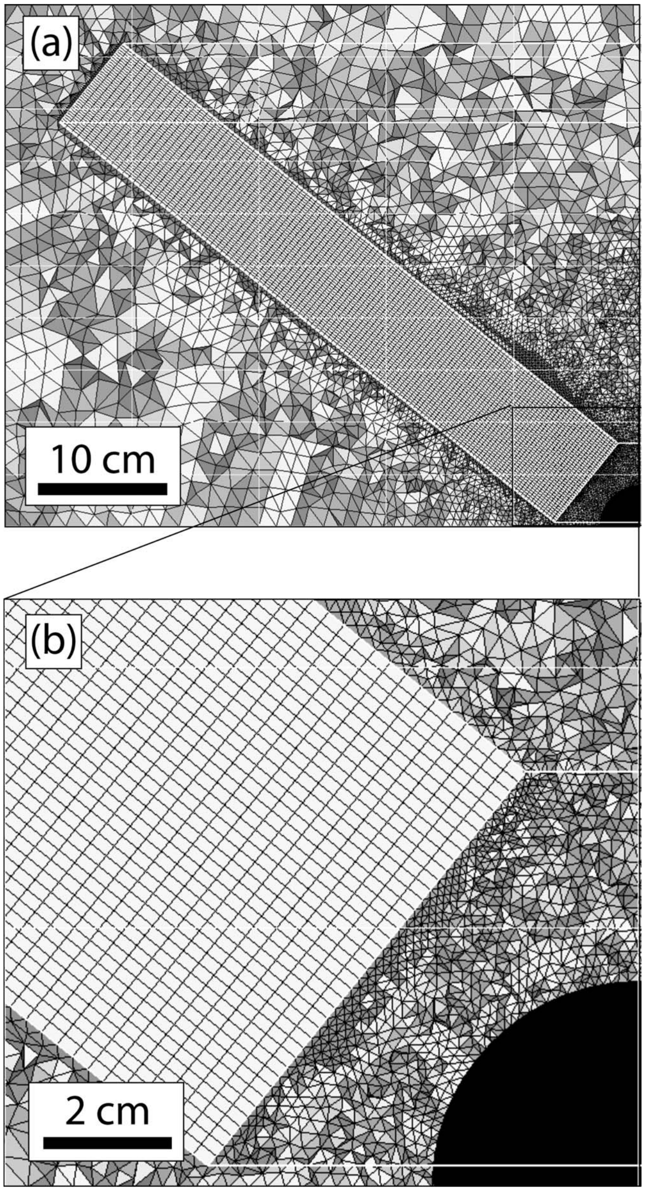

FIG. 2. A 2D slice through the 3D computational domain, where the shading corresponds to a 3D rendering of the computational tetrahedra nearest the vertical midplane. (a) A 2D cross section through the vertical midplane $y=0$. Only the left half of the domain ($x<0$) is shown; the right half is essentially a reflection about the vertical axis. The entire computational domain is 100 cm long $\times$ 100 cm wide $\times$ 45 cm high. The region with rectangular cells wraps around the vertical axis to create a conical region similar to those in Fig. 1. (b) A close-up of the region surrounding the half sphere. Grid size is 0.2 cm near the sphere (radius $R=3.25$ cm) and increases to 2 cm far from the generation region and wavebeams.

half sphere is situated with its center at the origin in a computational domain that is 100 cm long $\times$ 100 cm wide $\times$ 45 cm high. The conical wave propagation region is modeled with a rectangular structured grid rotated about the vertical axis, and the generation region surrounding the sphere is modeled with an unstructured tetrahedral grid (Fig. 2). The remaining volume, which consists mainly of the background barotropic flow, is also made up of unstructured tetrahedra with a characteristic size of up to 2 cm. The control volumes can be made very large in this region because the flow is uniform and large scale. The structured grid in the wave propagation region enables very fine control over the cross- and along-beam resolution. Since the wavebeam flow velocity varies much more rapidly in the cross-beam direction than in the along-beam direction, we can use different spatial resolutions in the two directions to maximize accuracy and minimize computational time. The unstructured grid in the generation region adapts the grid from the structured beam propagation zone to the curved boundary of the sphere. Despite all flows being laminar, high resolution is needed to accurately capture the flow field, where velocity can change markedly over a distance of a few percent of the sphere radius. The grids used for most of the results presented in this study contain roughly 5×10^6 control volumes. For all results presented here, the cross-beam resolution is 0.2 cm and the along-beam resolution varies from 0.3 cm near the generation region to 1 cm in the far field. The unstructured grid in the generation region is more difficult to characterize but there is a typical separation of 0.2 cm between computational nodes. We also used a more resolved grid in the boundary layer of the sphere, obtaining up to 0.015 cm resolution normal to the sphere, as described in the Appendix.

The stratification is such that the density at the top of the computational domain ($z=45$ cm) is equal to that of water, 1 g/cm^3. The density increases linearly with increasing depth, reaching a maximum value of 1.1035 g/cm^3 at the bottom ($z=0$). This gives a buoyancy frequency $N=1.50$ rad/s. An oscillating tidal flow $u(t)=A\omega\sin(\omega t)$ [with $\omega=0.942$ rad/s, which by Eq. (1) yields $\alpha=38.9°$] is enforced at the left and right boundaries of the computational domain. For simplicity in the simulations and experiments, the flow oscillates back and forth in a single direction, which is slightly different from the oceanographic forcing, where the barotropic flow follows an elliptical path due to the Coriolis force. The half sphere is a no-slip boundary, and the top, bottom, front, and back boundaries are free-slip walls. As will be discussed later, the bottom boundary is effectively a symmetry plane for the purposes of comparison with experiment.

Simulations are performed on the Lonestar cluster at the Texas Advanced Computing Center, typically using blocks of 128 processors. All simulations are run for at least seven forcing periods to ensure that steady state is reached. By the seventh period, the internal wave fields are within 1.3% of their asymptotic values; this is determined by examining the time series of velocity at points in the internal wave field. Consequently, all of the analyses were done on the seventh through tenth periods. At these times, reflections from boundaries have not had time to set up and interfere with the results. The shape and extent of the computational domain was chosen such that unwanted wave reflections would be in the regions below the conical wave characteristics, where they would not interfere with the analysis presented here. In addition, wave reflections are much weaker than in similar 2D studies because there is a $1/r$ geometrical spreading factor associated with 3D internal waves emanating from a localized source. This spreading factor, in addition to normal viscous dissipation and a suitably chosen domain, ensures that reflections do not interfere with the internal wave field.

While the simulations are conducted for a half sphere on

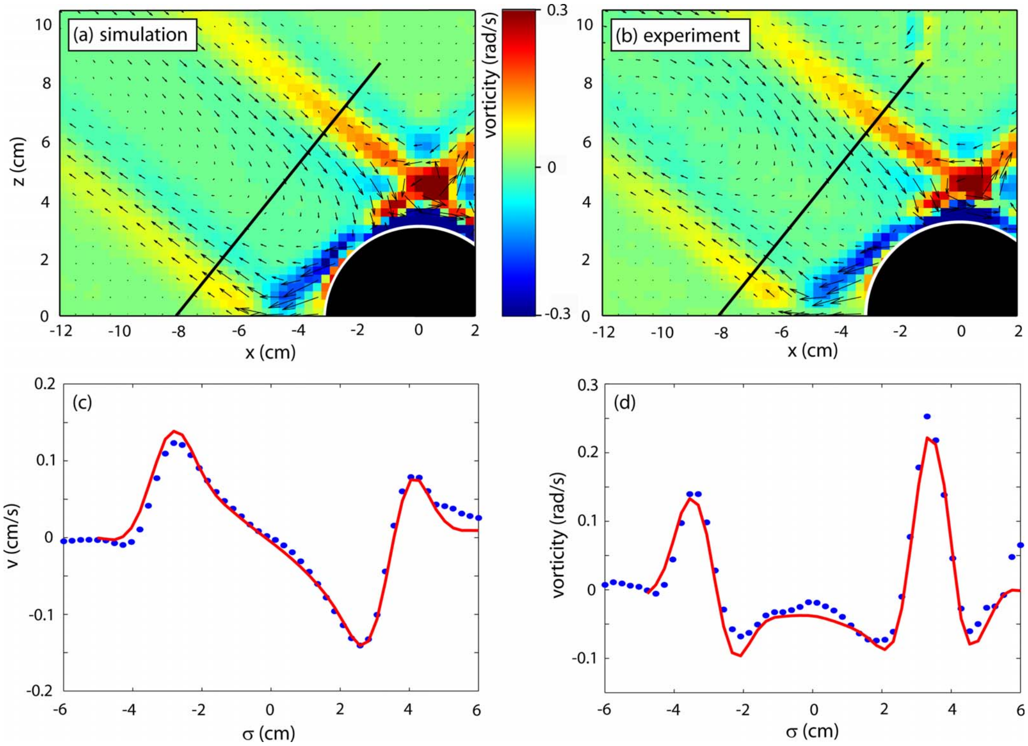

FIG. 3. (Color online) Instantaneous velocity field (arrows) and vorticity field (color) in the vertical midplane $y=0$ from (a) simulation and (b) experiment. These fields are displayed when the flow is moving to the right, 5% of a period after the velocity maximum. The lower graphs compare simulation (solid lines) and experiment (dots) at $r/R=2$ for instantaneous profiles of (c) velocity and (d) vorticity, along the black diagonal lines in (a) and (b). σ is the cross-beam coordinate, defined to be zero between the two wavebeams, and becoming positive toward the upper right. The forcing frequency is $\omega=0.942$ rad/s, which remains fixed for this study, and the forcing amplitude $A/R=0.092$. Profiles are only displayed for a single phase, but a similar quality of comparison between simulation and experiment is obtained at all phases and at other distances along the wavebeams.

a plane, the experiments are conducted (for practical reasons) for a whole sphere. To test for differences between the flows in the upper half domain for the two geometries we did simulations for both a whole sphere and for a half sphere on a free-slip plane. We found that in the upper half plane the wave velocity amplitude at $\phi=0$ differed by no more than 1% between the two simulations, verifying that the free-slip bottom boundary in the simulations effectively acts as a symmetry plane. This result justifies our comparison of observations of laboratory flow generated by a whole sphere with simulations for a half sphere.

B. Experiments

Experiments are performed in a glass tank 90 cm long $\times 45$ cm wide $\times 60$ cm high. The tank is filled with a linearly stratified salt solution using the double-bucket technique.[38] The fluid at the top is pure water and at the bottom is a salt solution with density 1.15 g/cm^3, which is larger than that at the bottom of the domain in the simulations (1.1035 g/cm^3) because the experimental vertical domain is larger; in both cases $N=1.50$ rad/s.

A nylon sphere with diameter 6.5 cm is mounted on a threaded rod and oscillated horizontally with a traverse mechanism mounted above the tank. The oscillation amplitude is 0.3 cm, giving a nondimensionalized forcing amplitude $A/R=0.092$, where $R=3.25$ cm is the radius of the half sphere.

Particle image velocimetry is used to obtain 2D velocity fields in a vertical plane passing through the center of the sphere. The fluid is seeded with titanium dioxide particles with size of 1–10 μm. These tracer particles are illuminated with a 1 W green laser beam spread into a 5 mm thick vertical light sheet. Images of the light sheet plane are obtained with a 10-bit digital camera with resolution 1004×997 and analyzed with the correlation image velocimetry software of Fincham and Delerce.[39] From the raw data, we obtain vector velocity fields on a 50×50 grid, corresponding to a spatial resolution of 0.28 cm. The experimental system is similar to our computational domain, except that the results are in the tide's reference frame rather than the half sphere's reference frame; a reference frame transformation allows direct comparison between the simulations and experiments.

III. LINEAR INTERNAL WAVES

A. Flow in the forcing direction

Figure 3 shows an example of the good agreement found between the experimental and numerical flow fields. The waves are bimodal near the sphere and are (in the plane defined by the forcing direction and the vertical axis through the center of the half sphere) similar to the internal wave field generated by a horizontally oscillating cylinder.[7] In Figs. 3(c) and 3(d), the σ-axis is defined to be perpendicular to the wave propagation direction, with positive sigma to-

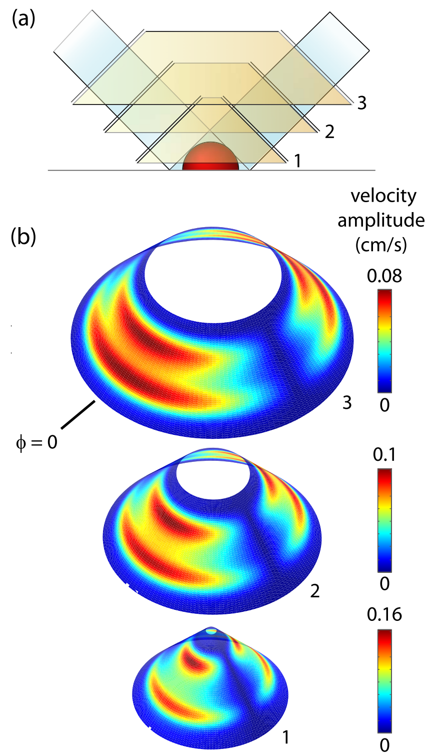

FIG. 4. (Color online) (a) A 2D cross section of conical surfaces where the wave amplitude is visualized at (1) $r=2R$, (2) $3.5R$, and (3) $5R$ from the center of the half sphere, for forcing amplitude $A/R=0.092$. (b) The velocity amplitude on the three conical surfaces (displaced vertically for visualization) is denoted by shading, which is different for each surface to enhance the visibility of the wave structure at each distance.

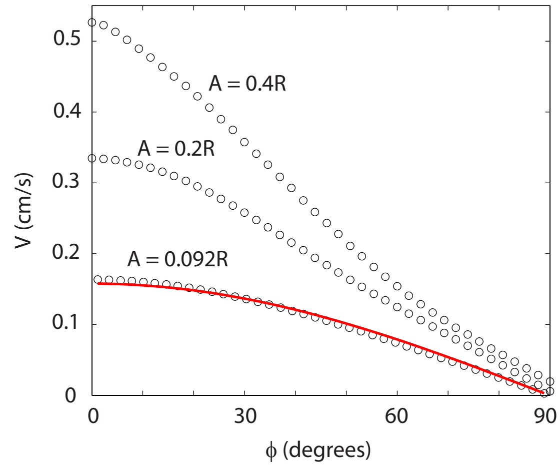

FIG. 5. (Color online) The azimuthal dependence of the wave field at $r=2R$ simulated at low forcing amplitude ($A/R=0.092$) follows the $\cos \phi$ prediction of inviscid theory (solid curve). For higher forcing, the wavebeams become stronger in the forcing direction ($\phi=0$) and there is large deviation from the linear inviscid theory.

ward the upper right. The origin of the σ coordinate is along a line extending from the center of the half sphere along the wave propagation angle.

B. Wave structure

Figure 4 is an example of a flow field visualized in three dimensions, on a conical surface so that wave strength can be seen at all azimuthal angles for a given distance from the center of the half sphere. These results are obtained by fitting a sine wave with frequency ω to the time series of the along-beam velocity component at every point on each surface. As expected, the internal waves are radiated most strongly in the forcing direction, with the waves becoming less intense with increasing azimuthal angle. Near the sphere the wavebeam is bimodal; the top beam propagates directly outward from the half sphere, while the bottom beam is reflected from the bottom boundary. Further from the sphere, viscous effects begin to smear these two distinct waves. By $r=5R$ the waves already have significant overlap and at large r the structure becomes unimodal.

To characterize the azimuthal dependence of the internal wave field, we plot the maximum along-beam velocity amplitude of the upper beam as a function of azimuthal angle for three forcing amplitudes (Fig. 5). For the smallest forcing, the wave amplitude is described well by a cosine dependence, as predicted by the linear inviscid analysis of Appleby and Crighton.[34] For higher forcing, the behavior departs from linear theory: A higher proportion of the wave energy is radiated in the forcing direction. To quantify the energy radiation as a function of azimuthal angle, we evaluate energy flux associated with the internal waves in the far field. For low wave amplitude, we use the linear energy flux term $p'\vec{u}'$, where $\vec{u}'$ is the baroclinic velocity and p' is the baroclinic component of the pressure perturbation. Near the half sphere, it is unclear how to distinguish between the barotropic and baroclinic components of the velocity and pressure fields. However, in the far field ($r \gg R$), we use the fact that the barotropic tidal flow is, to first order, unperturbed by the presence of the half sphere. For a spatially uniform oscillatory background flow, $u(t)=A\omega \sin(\omega t)$, it can be shown using the Navier–Stokes equation that the barotropic component of the pressure perturbation is a function only of x and t,

$$p'_{bt}(x) = (-A\omega^2 \cos \omega t)x. \tag{7}$$

This barotropic pressure is subtracted from the pressure perturbation from the simulations to obtain the baroclinic pressure perturbation associated with the internal waves. When multiplied by the baroclinic velocity, this gives the energy flux at a point in the internal wave. Energy flux is summed in the cross-beam direction and averaged over a single period to obtain the average energy radiation as a function of the azimuthal angle ϕ. At low amplitude ($A/R=0.1$) the ϕ-dependence of the radiated energy is described well by a $\cos^2 \phi$ function, as would be expected since the beam velocity and barotropic pressure perturbation should both scale as $\cos \phi$; 50% of the radiated energy is within 23° of the forcing direction. At higher amplitudes, a greater fraction of the total radiated energy is closer to the forcing direction (cf. Fig. 5).

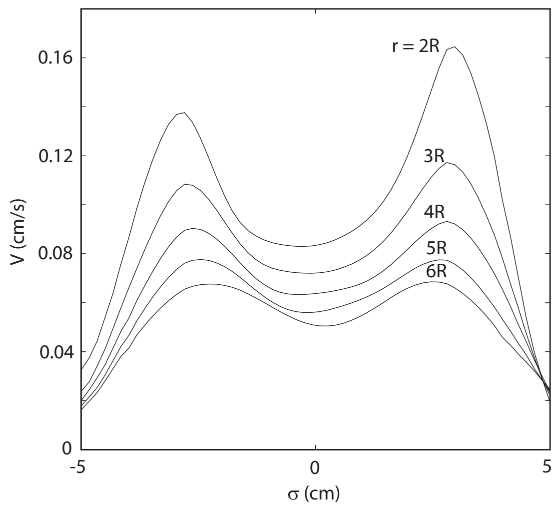

FIG. 6. Cross-beam profiles of the along-beam velocity component at $r/R=2$, 3, 4, 5, and 6, where R is the radius of the half sphere. These profiles are taken in the forcing direction ($\phi=0$) at a forcing amplitude of $A/R=0.092$. At distance $2R$ from the center of the half sphere, the ratio of velocity amplitudes in the two beams is 1.23, but this ratio drops with distance along the beam, and the beams are equal in amplitude by $r=5R$.

C. Asymmetry between the upper and lower wavebeams

Simulations and experiments both show an asymmetry between the upper and lower wavebeams generated by the sphere (Fig. 6), as can be seen in Fig. 8(a) of the paper on experiments by Flynn *et al.*[29] The asymmetry appears to be a 3D effect because no 2D studies have reported any asymmetry.

The asymmetry in the velocity amplitudes of the two wave beams follows from a geometrical argument. A half sphere (or any supercritical topography) generates internal wave beams along two nested conical characteristics, as in Fig. 1(b). Waves along the inner characteristic cone propagate upward from the near-critical regions on the half sphere, and waves along the outer characteristic also propagate upward after being reflected from the bottom boundary. By symmetry, equal amounts of energy go into each wavebeam.

A cross section such as those in Fig. 4 intersects each characteristic surface in a circle. Viewed from the side, the circles of intersection are the horizontal lines in Fig. 7. In the inviscid limit (with attenuation neglected), the energy flux in each wavebeam should be inversely proportional to the circumference of the circle of intersection of the cross section and the characteristics. This is a consequence of the wavebeam spreading out in three dimensions, similar to the geometrical focusing discussed in Ref. 40. This relationship between energy fluxes F_1 and F_2 in the two wavebeams can be written as

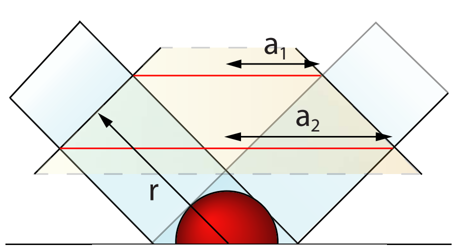

FIG. 7. (Color online) A 2D cross section illustrating the observed wavebeam asymmetry. For a given cross section distance, the energy in the top beam is concentrated in a smaller area (a circle with radius a_1) than the energy in the lower beam (a circle with radius a_2). The upper wavebeam therefore has a higher energy density and, consequently, a higher amplitude than the lower beam. As r becomes larger, the ratio of a_1 to a_2 approaches 1, and the asymmetry decreases correspondingly.

$$\frac{F_1}{F_2} = \frac{a_2}{a_1}, \tag{8}$$

where the radii a_1 and a_2 are defined in Fig. 7. Geometrical considerations allow us to rewrite this as

$$\frac{F_1}{F_2} = \frac{r/R + \tan\alpha}{r/R - \tan\alpha}, \tag{9}$$

where α is defined in Eq. (1). This function has the expected qualitative behavior: The ratio of energy fluxes approaches 1 for large r/R and diverges as r/R approaches $\tan\alpha$. To make a quantitative comparison to simulation data, we use the result that wavebeam energy flux is related to energy density by the expression[41]

$$\vec{F} = \vec{c_g} E, \tag{10}$$

where $\vec{c_g}$ is the group velocity and E is the energy density of the wave. In general, wavebeams are comprised of a spectrum of wavenumbers with different group velocities, but in both simulations and experiments, we observe a distinct wave front propagating outward from the half sphere after the onset of oscillation, implying a sharply peaked wavenumber spectrum around a dominant wavenumber, which determines the group and phase velocities of the waves. It is assumed that the two wavebeams under consideration have the same dominant wavenumber, and therefore the same group velocity $\vec{c_g}$. The wavebeam energy density is proportional to the wave amplitude squared, and Eq. (10) is used in the second equality to show that the ratio of beam amplitudes is then

$$\frac{A_1}{A_2} = \sqrt{\frac{E_1}{E_2}} = \sqrt{\frac{r/R + \tan\alpha}{r/R - \tan\alpha}}. \tag{11}$$

To compare Eq. (11) to numerical results, we compute the ratio of beam strengths using the maximum beam amplitudes of the upper and lower wave beams at several distances from the center of the half sphere. The error bars are based on the standard error associated with fitting a sine function at the forcing frequency to a time series of beam velocities at an output of 20 points per period. We find that Eq. (11) predicts the asymmetry well for large r/R (Fig. 8), where linear inviscid theory applies, but the measurements depart from the prediction for small r/R where beam-beam and beam-boundary layer interactions can be important. As discussed in Ref. 29 the interactions between the generated internal waves and the viscous boundary layer around the half sphere are not well understood, and we show in Sec. IV the importance of nonlinear effects near the half sphere. In the

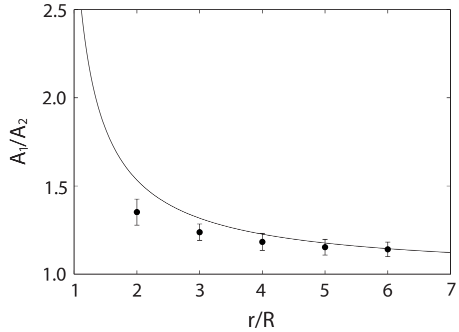

FIG. 8. Comparison of measurements (solid dots) of the wavebeam asymmetry (ratio of the upper to lower wavebeam amplitudes) from a simulation with prediction (11) from a geometrical argument (solid curve). ($A/R=0.4$).

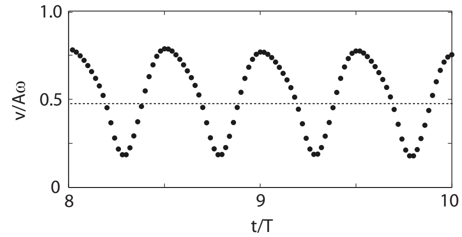

FIG. 10. The flow perpendicular to the forcing direction varies in strength periodically at frequency 2ω. The y component of velocity is plotted here for a position 0.2 cm above a half sphere of radius $R=3.25$ cm at $\phi=90°$ and $\theta=38.9°$; this is the center of the near-critical region, where the motion perpendicular to the forcing direction is strongest. Note that the average of the y component of velocity (given by the dotted line) is nonzero.

near field, both of the above complicating factors reduce the validity of the symmetry assumptions used to derive the geometrical argument (11).

IV. NONLINEAR OUT-OF-FORCING-PLANE FLOW

The experiments and simulations both reveal a strong flow *perpendicular* to the forcing direction (i.e., in the y direction); we refer to this as the nonlinear flow. Fluid immediately above the sphere is pushed downward along the $\phi=90°$ directions in narrow boundary layers. This flow departs near $\theta=\alpha$ [as defined in Eq. (1)] from the boundary layer and propagates outward in the y direction. Snapshots from experiment and simulation show the same out-of-forcing-plane flow (Fig. 9). The speed of the downward flow in the boundary layer (at $\phi=90°$) is roughly equal to the maximum forcing speed, $A\omega$.

We verify that the flow perpendicular to the forcing direction is unique to internal waves by performing experiments with a forcing frequency higher than the buoyancy frequency, so internal waves do not propagate. Then the flow simply deforms around the oscillating sphere. The out-of-forcing-plane flow arises from wavefronts that travel in the $y=0$ plane and collide near the top of the sphere, generating a flow that is predominately at twice the forcing frequency (Fig. 10); the y-component of velocity is always positive, meaning that the flow is moving down the side of the sphere at all times.

In this study, we have intentionally made $2\omega > N$ so that second harmonic waves are not allowed to propagate. However, as can be seen in Fig. 10, strong motion at twice the forcing frequency is still present near the half sphere. Thus a large amount of energy cannot propagate away from the half sphere, resulting in trapped energy that may contribute to local mixing near the sides of the topography. The trapped energy can be estimated using the wave saturation data (circles) in Fig. 11. The internal wave field begins to saturate at $A/R=0.3$ so the wave energy remains roughly fixed at higher forcing amplitudes even though more energy is being supplied by the forcing. At $A/R=0.6$, the maximum wave amplitude is 0.32 cm/s, which is only 70% of the value ex-

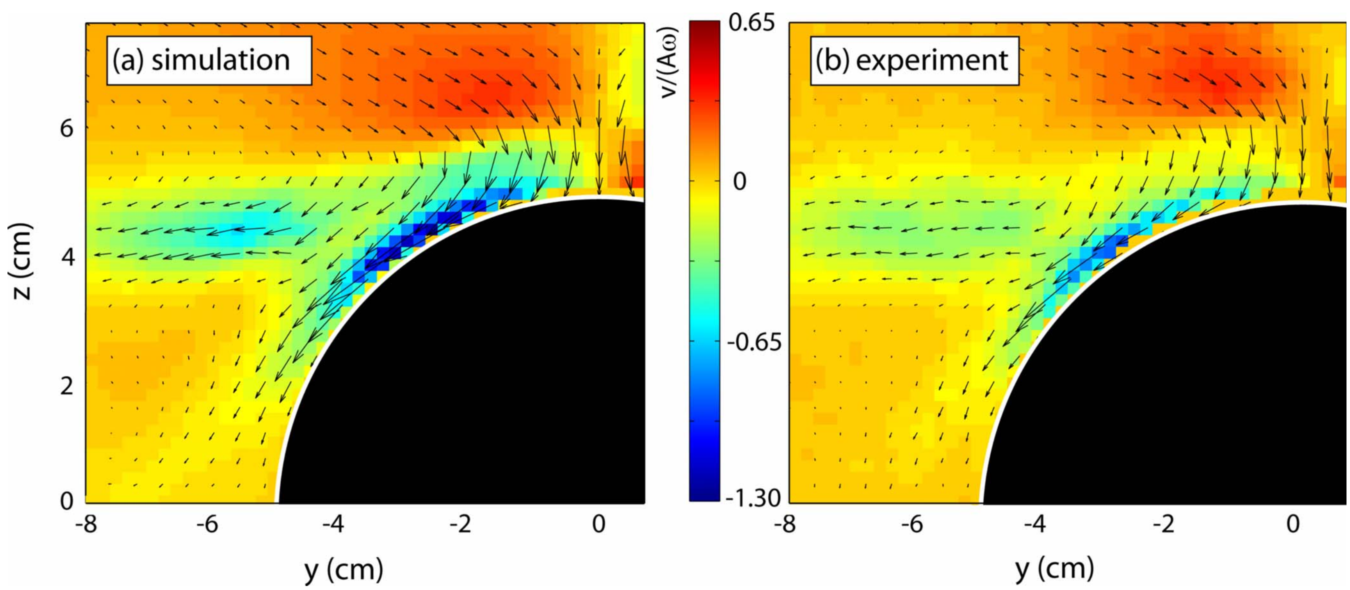

FIG. 9. (Color online) An intense boundary layer current and an outflow perpendicular to the forcing direction is revealed by these snapshots, where the forcing is normal to the page ($R=5$ cm and amplitude $A/R=0.2$). The shading represents the y component of velocity relative to the maximum forcing velocity, $A\omega$.

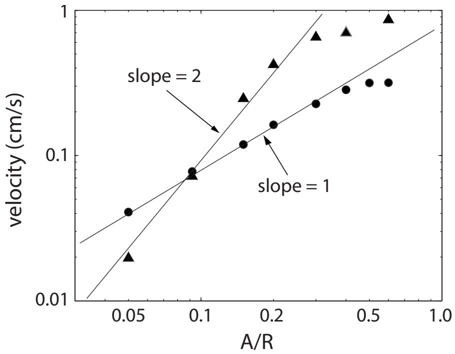

FIG. 11. At low forcing amplitude, the flow velocity perpendicular to the forcing direction (triangles) varies as the forcing amplitude squared, indicating this flow arises from nonlinear interactions. In contrast, the internal wave velocity amplitude (circles) in the forcing plane increases linearly with forcing amplitude, as expected from linear inviscid theory, while for higher forcing ($A/R \gtrsim 0.3$), the velocity amplitude saturates (at 0.32 cm/s). The mean flow is computed 0.2 cm above the surface of the half sphere at azimuthal angle $\phi=90°$ and polar angle $\theta=\alpha$. The wave amplitudes are the maximum along-beam velocity amplitudes of the top wave beams at $r/R=5$ ($R=3.25$ cm). The uncertainties (less than 3%) are small compared to the size of the data points.

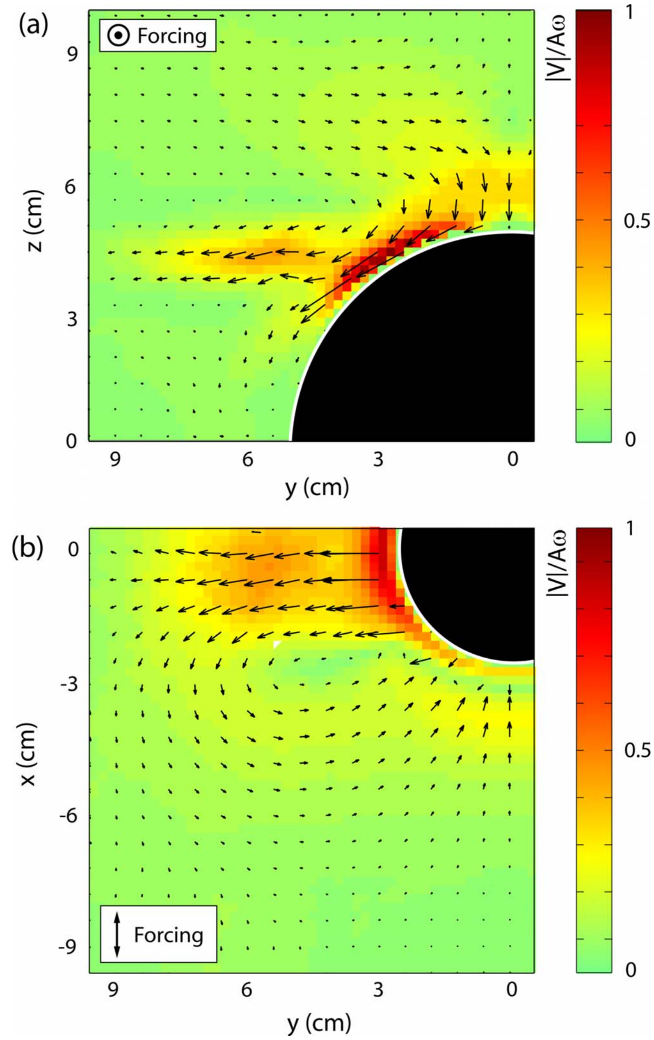

FIG. 12. (Color online) (a) Flow perpendicular to the vertical forcing plane is revealed by this plot of the average velocity field in the plane through the sphere center ($x=0$). There is a strong flow outward along the y-axis. (In this figure, in-plane velocities are denoted by vectors and in-plane speeds by shading.) (b) In the horizontal plane at $z=4.25$ cm, one can see that the flow forms a closed circulation, returning to the sphere in the forcing direction ($R=5$ cm).

trapolated from lower forcing amplitudes in the linear regime (see Fig. 11). Since kinetic energy is proportional to the square of velocity, roughly 50% of the energy extracted from the tide is not propagating away in the form of internal waves.

The zero frequency component of the flow perpendicular to the forcing direction is plotted as a function of forcing amplitude in Fig. 11. For small forcing amplitude ($A/R \lesssim 0.2$), the velocity amplitude is proportional to the square of the forcing amplitude, as would be expected for a nonlinear process. For comparison, the figure also shows the internal wave amplitude in the forcing plane; this velocity depends linearly on the forcing amplitude (for low forcing).

The average nonlinear flow in both the vertical forcing plane through the sphere center and through a horizontal plane above the sphere center is shown in Fig. 12. Strong flow down the sides of the sphere in the direction perpendicular to the forcing is evident in Fig. 12(a); the velocity amplitude is comparable to the forcing velocity amplitude, $A\omega$. Most of the boundary flow splits off and moves in the y direction. This outward flow, viewed from above in Fig. 12(b), recirculates in the horizontal plane, impinging on the half sphere from the $\phi=0$ direction. This circulation is not entirely within the horizontal plane but the vertical length scale of the circulation is very small compared to the horizontal length scale (roughly 0.5 and 10 cm, respectively). This is expected due to the suppression of vertical motion by the stratification.

V. DISCUSSION

We have studied the internal wave generation process in numerical simulations and experiments for a model for tidal flow over 3D seamounts. Our model is a horizontally oscillating stratified flow past a half sphere on a plane.

In the forcing plane ($\phi=0$), we find that the internal wave field is qualitatively similar to the 2D internal wave field generated by an oscillating cylinder. For flow over a half sphere, the wave amplitude decreases with increasing angle ϕ away from the forcing direction and becomes zero perpendicular to the forcing direction. For low forcing amplitude, the wave field follows the angular dependence of the linear inviscid theory of Applyby and Crighton.[34] However, for $A/R > 0.2$ there are large deviations from that theory, and a larger fraction of the radiated energy is in the forcing direction. This is consistent with the previous work of Munroe and Lamb[32] and Holloway and Merrified,[31] who found that despite the three dimensionality of the topography, most of the internal wave energy is radiated in the tidal forcing direction.

Wave radiation at large angles to the forcing direction is weak, but we have discovered that the 3D topography produces, surprisingly, a strong flow in the plane perpendicular to the oscillating tidal flow. This perpendicular flow is a prominent effect, producing flow speeds comparable to the

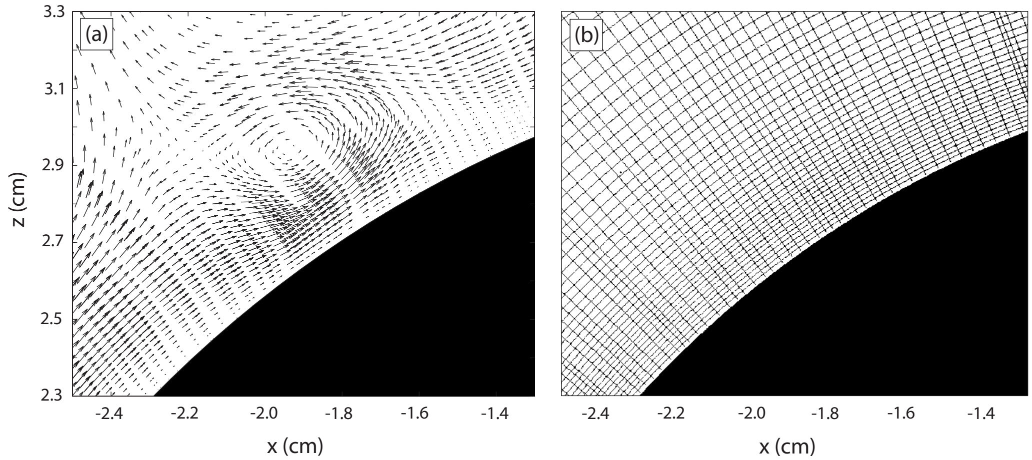

FIG. 13. (a) Instantaneous velocity field in the $y=0$ plane, when the sphere was at its rightmost position at zero velocity. There are about ten vectors in the boundary layer; the grid used in computing this flow is shown in (b). The vortex discernible in (a) is a short-lived structure that forms when the flow in the generation region changes direction. The vectors are not regularly spaced since the data have not been interpolated to a regular grid.

tidal flow speed. For low forcing, the perpendicular flow speed is proportional to the square of the forcing amplitude, indicating that this flow is a result of nonlinear interactions, probably between the internal waves being generated or between internal waves and the viscous boundary layer. In the ocean, strong flow perpendicular to a tidal flow could enhance material transport and mixing near bottom topography. Since the perpendicular flow is proportional to the square of the forcing amplitude, this flow will be especially strong near topography with small features (where the excursion parameter A/R will be large). In addition to a nonzero mean component, the nonlinear flow has a large component that oscillates at twice the forcing frequency, leading to the possibility of strong out-of-forcing-plane second harmonics when $2\omega < N$. This suggests that a significant fraction of the energy converted from the barotropic tide by bottom topography could be radiated in the direction perpendicular to the forcing.

Although linear theory and 2D simulations are good predictors of linear internal wave generation, we find that strong flows arise due to the three dimensionality of bottom topography. Our results should apply widely because even quasi-2D topographic features such as ridges have 3D roughness and ends where 3D effects can be significant. These effects manifest themselves across the entire excursion parameter range examined in this work, $0.05 < A/R < 0.6$, with the lower end of the range applying to large bottom topography, and the higher end being more relevant to small topography or to 3D roughness on large topography.

ACKNOWLEDGMENTS

The authors thank Frank Ham for access and advice on the CDP code, and Robert Moser, Philip Marcus, Chung-Hsiang Jiang, and Omar Lopez for useful discussions. In addition, the authors wish to thank Bruno Voisin for useful correspondence regarding comparison to his recent theoretical work. This research was supported by the National Science Foundation, Chemical, Bioengineering, Environmental, and Transport Systems Program (Award No. 0755114). The Texas Advanced Computing Center (TACC) at The University of Texas at Austin provided high performance computing resources.

APPENDIX: VERIFICATION OF NUMERICAL CODE

CDP has been verified and validated in different contexts.[42,43] In our work we validated the code by comparison to experiment in Sec. III. In addition, we undertook a grid convergence study on the simulations. This is not easy with an unstructured grid where the grid spacing is nonuniform. We were particularly concerned whether the half sphere's boundary flow was fully resolved. The thickness of the Stokes boundary layer on the half sphere is $\delta = \sqrt{(2\nu/\omega)} \simeq 0.15$ cm. To ensure full resolution of this boundary layer, we covered the half sphere surface with triangles with 0.05 cm characteristic nodal separation instead of the 0.2 cm nodal separation used in the calculations in the rest of the paper. We then extruded the 0.05 cm mesh outward in the sphere-normal direction at intervals of 0.015 cm, resulting in about ten control volumes within the boundary layer. An example of the boundary layer flow computed with this mesh is shown in Fig. 13.

Additional grids were generated with the boundary layer resolution getting progressively coarser: The grids had sphere-normal resolutions of 0.015, 0.030, and 0.060 cm (0.5%, 1%, and 2% of R, respectively). Other than the differing resolutions in the sphere boundary layer, the three grids were nearly identical. In particular, the structured grid in the wave propagation region remained unchanged. Simulations were run on all three grids at a relatively high forcing amplitude ($A=0.4$, $R=1.3$ cm) at the same frequency used in the rest of this study ($\omega=0.942$ rad/s). To ensure numerical stability, a time step of $\Delta t = T/2000$ was used for all three simulations, where $T=(2\pi/\omega)$ is the forcing period.

We use a single scalar quantity to compare between grids, the along-beam velocity amplitude integrated over conical surfaces such as those in Fig. 4. The integrated scalar quantity corresponds to a total material flux amplitude per period associated with the wave motion. For the cases of the three grids, integrating over the velocity amplitude at distance $r=4R$ yields the following results:

Grid	Coarse	Medium	Fine
Value	92.117	94.214	95.620

Although the integrated velocity amplitude is converging with increased resolution, the convergence is not rapid enough to be second order in space. This is not surprising, however, since we only refined the grid in the region immediately surrounding the sphere, rather than refining the grid by progressive factors of 2 at all locations in the domain.

To check the numerical results obtained using the less refined grid shown in Fig. 2, we compare cross sections of the internal wave beams in this grid and with the grids with highly refined boundary layers. At forcing amplitude $A/R=0.4$, the internal wave velocity amplitudes differ by at most 4%. We conclude that fully resolving the boundary layer around the sphere is not critical to understand the generated internal waves. In conclusion, we have high confidence in our simulation results, based on the good comparison with experiments (Fig. 3) and the results obtained for boundary layers with different mesh sizes.

[1]W. Munk and C. Wunsch, "Abyssal recipes II: Energetics of tidal and wind mixing," Deep-Sea Res., Part I **45**, 1977 (1998).
[2]G. D. Egbert and R. D. Ray, "A significant dissipation of tidal energy in the deep ocean inferred from satellite altimeter data," Nature (London) **405**, 775 (2000).
[3]L. St. Laurent and C. Garrett, "The role of internal tides in mixing the deep ocean," J. Phys. Oceanogr. **32**, 2882 (2002).
[4]C. Wunsch and R. Ferrari, "Vertical mixing, energy and the general circulation of the oceans," Annu. Rev. Fluid Mech. **36**, 281 (2004).
[5]C. Wunsch, "The work done by the wind on the oceanic general circulation," J. Phys. Oceanogr. **28**, 2332 (1998).
[6]D. G. Hurley and G. Keady, "The generation of internal waves by vibrating elliptic cylinders. Part 2. Approximate viscous solution," J. Fluid Mech. **351**, 119 (1997).
[7]H. P. Zhang, B. King, and H. L. Swinney, "Experimental study of internal gravity waves generated by supercritical topography," Phys. Fluids **19**, 096602 (2007).
[8]T. Peacock, P. Echeverri, and N. J. Balmforth, "An experimental investigation of internal tide generation by two-dimensional topography," J. Phys. Oceanogr. **38**, 235 (2008).
[9]L. Gostiaux and T. Dauxois, "Laboratory experiments on the generation of internal tidal beams over steep slopes," Phys. Fluids **19**, 028102 (2007).
[10]L. Gavrilov and T. Ermanyuk, "Internal waves generated by circular translational motion of a cylinder in a linearly stratified fluid," J. Appl. Mech. Tech. Phys. **38**, 224 (1997).
[11]N. J. Balmforth, G. R. Ierley, and W. R. Young, "Tidal conversion by subcritical topography," J. Phys. Oceanogr. **32**, 2900 (2002).
[12]E. Di Lorenzo, W. R. Young, and S. Llewellyn Smith, "Numerical and analytical estimates of M_2 tidal conversion at steep oceanic ridges," J. Phys. Oceanogr. **36**, 1072 (2006).
[13]L. St. Laurent, S. Stringer, C. Garrett, and D. Perrault-Joncas, "The generation of internal tides at abrupt topography," Deep-Sea Res., Part I **50**, 987 (2003).
[14]S. Legg and K. M. H. Huijts, "Preliminary simulations of internal waves and mixing generated by finite amplitude tidal flow over isolated topography," Deep-Sea Res., Part II **53**, 140 (2006).
[15]S. Legg and J. Klymak, "Internal hydraulic jumps and overturning generated by tidal flow over a tall steep ridge," J. Phys. Oceanogr. **38**, 1949 (2008).
[16]F. Petrelis, S. Llewellyn Smith, and W. R. Young, "Tidal conversion at a submarine ridge," J. Phys. Oceanogr. **36**, 1053 (2006).
[17]S. G. Llewellyn Smith and W. R. Young, "Tidal conversion at a very steep ridge," J. Fluid Mech. **495**, 175 (2003).
[18]H. P. Zhang, B. King, and H. L. Swinney, "Resonant generation of internal waves on a model continental slope," Phys. Rev. Lett. **100**, 244504 (2008).
[19]S. Khatiwala, "Generation of internal tides in an ocean of finite depth: Analytical and numerical calculations," Deep-Sea Res., Part I **50**, 3 (2003).
[20]K. G. Lamb, "Energy and pseudoenergy flux in the internal wave field generated by tidal flow over topography," Cont. Shelf Res. **27**, 1208 (2007).
[21]S. M. Jachec, O. B. Fringer, M. G. Gerritsen, and R. L. Street, "Generation of internal tides in an ocean of finite depth: Analytical and numerical calculations," Geophys. Res. Lett. **33**, L12605, doi:10.1029/2006GL026314 (2006).
[22]M. A. Merrifield and P. E. Holloway, "Model estimates of M-2 internal tide energetics at the Hawaiian Ridge," J. Geophys. Res. **107**, 3179, doi:10.1029/2001JC000996 (2002).
[23]M. A. Merrifield, P. E. Holloway, and T. M. S. Johnston, "The generation of internal tides at the Hawaiian Ridge," Geophys. Res. Lett. **28**, 559, doi:10.1029/2000GL011749 (2001).
[24]J. D. Nash, E. Kunze, C. M. Lee, and T. B. Sanford, "Structure of the baroclinic tide generated at Kaena Ridge, Hawaii," J. Phys. Oceanogr. **36**, 1123 (2006).
[25]D. L. Rudnick, T. J. Boyd, R. E. Brainard, G. S. Carter, G. D. Egbert, M. C. Gregg, P. E. Holloway, J. M. Klymak, E. Kunze, C. M. Lee, M. D. Levine, D. S. Luther, J. P. Martin, M. A. Merrifield, J. N. Moum, J. D. Nash, R. Pinkel, L. Rainville, and T. B. Sanford, "From tides to mixing along the Hawaiian ridge," Science **301**, 355 (2003).
[26]C. M. Lee, E. Kunze, T. B. Sanford, J. D. Nash, M. A. Merrifield, and P. E. Holloway, "Internal tides and turbulence along the 3000-m isobath of the Hawaiian Ridge," J. Phys. Oceanogr. **36**, 1165 (2006).
[27]R. Dewey, D. Richmond, and C. Garrett, "Stratified tidal flow over a bump," J. Phys. Oceanogr. **35**, 1911 (2005).
[28]D. E. Mowbray and B. S. H. Rarity, "A theoretical and experimental investigation of the phase configuration of internal waves of small amplitude in a density stratified liquid," J. Fluid Mech. **28**, 1 (1967).
[29]M. R. Flynn, K. Onu, and B. R. Sutherland, "Internal wave excitation by a vertically oscillating sphere," J. Fluid Mech. **494**, 65 (2003).
[30]T. Peacock and P. Weidman, "The effect of rotation on conical wave beams in a stratified fluid," Exp. Fluids **39**, 32 (2005).
[31]P. E. Holloway and M. A. Merrifield, "Internal tide generation by seamounts, ridges, and islands," J. Geophys. Res. **104**, 25937, doi:10.1029/1999JC900207 (1999).
[32]J. R. Munroe and K. G. Lamb, "Topographic amplitude dependence of internal wave generation by tidal forcing over idealized three-dimensional topography," J. Geophys. Res. **110**, C02001, doi:10.1029/2004JC002537 (2005).
[33]P. G. Baines, "Internal tide generation by seamounts," Deep-Sea Res., Part I **54**, 1486 (2007).
[34]J. C. Appleby and D. G. Crighton, "Internal gravity-waves generated by oscillations of a sphere," J. Fluid Mech. **183**, 439 (1987).
[35]F. Ham and G. Iaccarino, "Energy conservation in collocated discretization schemes on unstructured meshes," in *Annual Research Briefs* (Center for Turbulence Research, Stanford, CA, 2004), pp. 3–14 (http://ctr.stanford.edu/ResBriefs04/ham_iaccarino.pdf).
[36]K. Mahesh, G. Constantinescu, and P. Moin, "A numerical method for large-eddy simulation in complex geometries," J. Comput. Phys. **197**, 215 (2004).
[37]F. Ham, K. Mattsson, and G. Iaccarino, "Accurate and stable finite volume operators for unstructured flow solvers," in *Annual Research Briefs* (Center for Turbulence Research, Stanford, CA, 2006), pp. 243–261 (http://ctr.stanford.edu/ResBriefs06/19_ham1.pdf).
[38]G. Oster, "Density gradients," Sci. Am. **213**, 70 (1965).
[39]A. Fincham and G. Delerce, "Advanced optimization of correlation imaging velocimetry algorithms," Exp. Fluids **29**, S013 (2000).
[40]O. Buhler and C. J. Muller, "Instability and focusing of internal tides in the deep ocean," J. Fluid Mech. **588**, 1 (2007).
[41]P. K. Kundu and I. M. Cohen, *Fluid Mechanics* (Elsevier Academic, New York, 2004).
[42]K. Mahesh, G. Constantinescu, S. Apte, G. Iaccarino, F. Ham, and P. Moin, "Large-eddy simulation of reacting turbulent flows in complex geometries," ASME J. Appl. Mech. **73**, 374 (2006).
[43]L. Shunn and F. Ham, "Method of manufactured solutions applied to variable-density flow solvers," in *Annual Research Briefs* (Center for Turbulence Research, Stanford, CA, 2007), pp. 155–168 (http://ctr.stanford.edu/ResBriefs07/14_shunn_pp155_168.pdf).